Analytical model for quantitative prediction of material contrasts in scattering-type near-field optical microscopy

A. Cvitkovic, N. Ocelic and R. Hillenbrand

Nano-Photonics Group, Max-Planck-Institut für Biochemie, 82152 Martinsried, Germany

nocelic@tum.de

Abstract: Nanometer-scale mapping of complex optical constants by scattering-type near-field microscopy has been suffering from quantitative discrepancies between the theory and experiments. To resolve this problem, a novel analytical model is presented here. The comparison with experimental data demonstrates that the model quantitatively reproduces approach curves on a Au surface and yields an unprecedented agreement with amplitude and phase spectra recorded on a phonon-polariton resonant SiC sample. The simple closed-form solution derived here should enable the determination of the local complex dielectric function on an unknown sample, thereby identifying its nanoscale chemical composition, crystal structure and conductivity.

OCIS codes: (110.3080) Infrared Imaging; (120.5820) Scattering Measurements; (180.5810) Scanning Microscopy; (300.6340) Spectroscopy, infrared

References

[1] F. Zenhausern, M. Oboyle, and H. Wickramasinghe, "Apertureless near-field optical microscope," Appl. Phys. Lett. **65**, 1623–1625 (1994).

[2] Y. Inouye and S. Kawata, "Near-field scanning optical microscope with a metallic probe tip," Opt. Lett. **19**, 159–161 (1994).

[3] A. Lahrech, R. Bachelot, P. Gleyzes, and A. C. Boccara, "Infrared-reflection-mode near-field microscopy using an apertureless probe with a resolution of lambda/600," Opt. Lett. **21**, 1315–1317 (1996).

[4] F. Keilmann and R. Hillenbrand, "Near-field microscopy by elastic light scattering from a tip," Philos. Trans. R. Soc. Lond. Ser. A-Math. Phys. Eng. Sci. **362**, 787–805 (2004).

[5] B. Knoll and F. Keilmann, "Near-field probing of vibrational absorption for chemical microscopy," Nature **399**, 134–137 (1999).

[6] O. J. F. Martin and C. Girard, "Controlling and tuning strong optical field gradients at a local probe microscope tip apex," Appl. Phys. Lett. **70**, 705–707 (1997).

[7] R. Fikri, D. Barchiesi, F. H'Dhili, R. Bachelot, A. Vial, and P. Royer, "Modeling recent experiments of apertureless near-field optical microscopy using 2D finite element method," Opt. Commun. **221**, 13–22 (2003).

[8] R. Esteban, R. Vogelgesang, and K. Kern, "Simulation of optical near and far fields of dielectric apertureless scanning probes," Nanotechnology **17**, 475–482 (2006).

[9] L. Novotny, E. J. Sanchez, and X. S. Xie, "Near-field optical imaging using metal tips illuminated by higher-order Hermite-Gaussian beams," Ultramicroscopy **71**, 21–29 (1998).

[10] T. Taubner, R. Hillenbrand, and F. Keilmann, "Performance of visible and mid-infrared scattering-type near-field optical microscopes," J. Microsc.-Oxf. **210**, 311–314 (2003).

[11] T. Taubner, R. Hillenbrand, and F. Keilmann, "Nanoscale polymer recognition by spectral signature in scattering infrared near-field microscopy," Appl. Phys. Lett. **85**, 5064–5066 (2004).

[12] M. B. Raschke, L. Molina, T. Elsaesser, D. H. Kim, W. Knoll, and K. Hinrichs, "Apertureless near-field vibrational imaging of block-copolymer nanostructures with ultrahigh spatial resolution," ChemPhysChem **6**, 2197–2203 (2005).

[13] M. Brehm, T. Taubner, R. Hillenbrand, and F. Keilmann, "Infrared spectroscopic mapping of single nanoparticles and viruses at nanoscale resolution," Nano Lett. **6**, 1307–1310 (2006).

[14] N. Ocelic and R. Hillenbrand, "Subwavelength-scale tailoring of surface phonon polaritons by focused ion-beam implantation," Nat. Mater. **3**, 606–609 (2004).

[15] A. Huber, N. Ocelic, T. Taubner, and R. Hillenbrand, "Nanoscale resolved infrared probing of crystal structure and of plasmon-phonon coupling," Nano Lett. **6**, 774–778 (2006).

[16] B. Knoll and F. Keilmann, "Infrared conductivity mapping for nanoelectronics," Appl. Phys. Lett. **77**, 3980–3982 (2000).

[17] J. S. Samson, G. Wollny, E. Brundermann, A. Bergner, A. Hecker, G. Schwaab, A. D. Wieck, and M. Havenith, "Setup of a scanning near field infrared microscope (SNIM): Imaging of sub-surface nano-structures in gallium-doped silicon," Phys. Chem. Chem. Phys. **8**, 753 – 758 (2006).

[18] A. Huber et al., "Simultaneous infrared material recognition and conductivity mapping by nanoscale near-field microscopy," Adv. Mater. (in press).

[19] J. Gersten and A. Nitzan, "Electromagnetic theory of enhanced Raman-scattering by molecules adsorbed on rough surfaces," J. Chem. Phys. **73**, 3023–3037 (1980).

[20] A. Wokaun, J. P. Gordon, and P. F. Liao, "Radiation damping in surface-enhanced Raman-scattering," Phys. Rev. Lett. **48**, 957 – 960 (1982).

[21] P. Aravind and H. Metiu, "The effects of the interaction between resonances in the electromagnetic response of a sphere-plane structure - applications to surface enhanced spectroscopy," Surf. Sci. **124**, 506–528 (1983).

[22] B. Knoll and F. Keilmann, "Enhanced dielectric contrast in scattering-type scanning near-field optical microscopy," Opt. Commun. **182**, 321–328 (2000).

[23] I. S. Averbukh, B. M. Chernobrod, O. A. Sedletsky, and Y. Prior, "Coherent near field optical microscopy," Opt. Commun. **174**, 33–41 (2000).

[24] F. Zenhausern, Y. Martin, and H. Wickramasinghe, "Scanning interferometric apertureless microscopy - optical imaging at 10 angstrom resolution," Science **269**, 1083–1085 (1995).

[25] M. B. Raschke and C. Lienau, "Apertureless near-field optical microscopy: Tip-sample coupling in elastic light scattering," Appl. Phys. Lett. **83**, 5089–5091 (2003).

[26] Z. H. Kim, B. Liu, and S. R. Leone, "Nanometer-scale optical imaging of epitaxially grown GaN and InN islands using apertureless near-field microscopy," J. Phys. Chem. B **109**, 8503–8508 (2005).

[27] R. Hillenbrand and F. Keilmann, "Material-specific mapping of metal/semiconductor/dielectric nanosystems at 10 nm resolution by backscattering near-field optical microscopy," Appl. Phys. Lett. **80**, 25–27 (2002).

[28] R. Hillenbrand, T. Taubner, and F. Keilmann, "Phonon-enhanced light-matter interaction at the nanometre scale," Nature **418**, 159–162 (2002).

[29] T. Taubner, F. Keilmann, and R. Hillenbrand, "Nanomechanical resonance tuning and phase effects in optical near-field interaction," Nano Lett. **4**, 1669–1672 (2004).

[30] L. Stebounova, B. B. Akhremitchev, and G. C. Walker, "Enhancement of the weak scattered signal in apertureless near-field scanning infrared microscopy," Rev. Sci. Instrum. **74**, 3670–3674 (2003).

[31] A. Cvitkovic, N. Ocelic, J. Aizpurua, R. Guckenberger, and R. Hillenbrand, "Infrared imaging of single nanoparticles via strong field enhancement in a scanning nanogap," Phys. Rev. Lett. **97**, (2006).

[32] J. L. Bohn, D. J. Nesbitt, and A. Gallagher, "Field enhancement in apertureless near-field scanning optical microscopy," J. Opt. Soc. Am. A-Opt. Image Sci. Vis. **18**, 2998–3006 (2001).

[33] J. Renger, S. Grafstrom, L. M. Eng, and R. Hillenbrand, "Resonant light scattering by near-field-induced phonon polaritons," Phys. Rev. B **71**, (2005).

[34] S. V. Sukhov, "Role of multipole moment of the probe in apertureless near-field optical microscopy," Ultramicroscopy **101**, 111–122 (2004).

[35] H. Hatano and S. Kawata, "Applicability of deconvolution and nonlinear optimization for reconstructing optical images from near-field optical microscope images," J. Microsc.-Oxf. **194**, 230 – 234 (1999).

[36] M. Labardi, S. Patane, and M. Allegrini, "Artifact-free near-field optical imaging by apertureless microscopy," Appl. Phys. Lett. **77**, 621–623 (2000).

[37] R. Hillenbrand and F. Keilmann, "Complex optical constants on a subwavelength scale," Phys. Rev. Lett. **85**, 3029–3032 (2000).

[38] J. N. Walford, J. A. Porto, R. Carminati, J. J. Greffet, P. M. Adam, S. Hudlet, J. L. Bijeon, A. Stashkevich, and P. Royer, "Influence of tip modulation on image formation in scanning near-field optical microscopy," J. Appl. Phys. **89**, 5159–5169 (2001).

[39] A. Wokaun, "Surface enhancement of optical-fields - mechanism and applications," Mol. Phys. **56**, 1 – 33 (1985).

[40] W. Denk and D. Pohl, "Near-field optics - microscopy with nanometer-size fields," J. Vac. Sci. Technol. B **9**, 510–513 (1991).

[41] N. Calander and M. Willander, "Theory of surface-plasmon resonance optical-field enhancement at prolate spheroids," J. Appl. Phys. **92**, 4878–4884 (2002).

[42] N. Ocelic, "Quantitative near-field phonon-polariton spectroscopy," Ph.D. thesis, Technical University Munich (2007).

[43] Y. C. Martin, H. F. Hamann, and H. K. Wickramasinghe, "Strength of the electric field in apertureless near-field optical microscopy," J. Appl. Phys. **89**, 5774–5778 (2001).

[44] C. F. Bohren and D. R. Huffman, *Absorption and Scattering of Light by Small Particles* (John Wiley & Sons Inc, 1998).

[45] J. D. Jackson, *Classical Electrodynamics* (Wiley & Sons, 1998).

[46] I. V. Lindell, G. Dassios, and K. I. Nikoskinen, "Electrostatic image theory for the conducting prolate spheroid," J. Phys. D-Appl. Phys. **34**, 2302–2307 (2001).

[47] D. V. Redzic, "An electrostatic problem - a point-charge outside a prolate dielectric spheroid," Am. J. Phys. **62**, 1118 – 1121 (1994).

[48] J. C. E. Sten and I. V. Lindell, "An electrostatic image solution for the conducting prolate spheroid," J. Electromagn. Waves Appl. **9**, 599 – 609 (1995).

[49] D. V. Redzic, "Image of a moving spheroidal conductor," Am. J. Phys. **60**, 506–508 (1992).

[50] Z. H. Kim and S. R. Leone, "High-resolution apertureless near-field optical imaging using gold nanosphere probes," J. Phys. Chem. B **110**, 19,804–19,809 (2006).

[51] J. Aizpurua, personal communication (2005).

[52] N. Ocelic, A. Huber, and R. Hillenbrand, "Pseudoheterodyne detection for background-free near-field spectroscopy," Appl. Phys. Lett. **89**, (2006).

[53] R. Bachelot, G. Wurtz, and P. Royer, "An application of the apertureless scanning near-field optical microscopy: imaging a GaAlAs laser diode in operation," Appl. Phys. Lett. **73**, 3333–3335 (1998).

[54] B. Knoll and F. Keilmann, "Electromagnetic fields in the cutoff regime of tapered metallic waveguides," Opt. Commun. **162**, 177–181 (1999).

[55] A. Huber, N. Ocelic, D. Kazantsev, and R. Hillenbrand, "Near-field imaging of mid-infrared surface phonon polariton propagation," Appl. Phys. Lett. **87**, (2005).

[56] F. Engelbrecht and R. Helbig, "Effect of crystal anisotropy on the infrared reflectivity of 6H-SiC," Phys. Rev. B **48**, 15,698 – 15,707 (1993).

[57] H. Mutschke, A. C. Andersen, D. Clement, T. Henning, and G. Peiter, "Infrared properties of SiC particles," Astron. Astrophys. **345**, 187–202 (1999).

[58] M. Hofmann, A. Zywietz, K. Karch, and F. Bechstedt, "Lattice-dynamics of SiC polytypes within the bond-charge model," Phys. Rev. B **50**, 13,401–13,411 (1994).

[59] H. Harima, S. Nakashima, and T. Uemura, "Raman-scattering from anisotropic LO-phonon-plasmon-coupled mode in n-type 4H-SiC and 6H-SiC," J. Appl. Phys. **78**, 1996–2005 (1995).

[60] I. V. Lindell, K. I. Nikoskinen, and M. J. Flykt, "Electrostatic image theory for an anisotropic half-space slightly deviating from transverse isotropy," Radio Sci. **31**, 1361 – 1368 (1996).

[61] I. V. Lindell, K. I. Nikoskinen, and A. Viljanen, "Electrostatic image method for the anisotropic half space," IEE Proc.-Sci. Meas. Technol. **144**, 156 – 162 (1997).

[62] S. C. Schneider, S. Grafstrom, and L. M. Eng, "Scattering near-field optical microscopy of optically anisotropic systems," Phys. Rev. B **71**, (2005).

[63] M. A. Ordal et al., "Optical properties of the metals Al, Co,Cu,Au,Fe,Pb,Ni,Pd,Pt,Ag,Ti and W in the infrared and far infrared," Appl. Opt. **22**, (1983).

1. Introduction

Apertureless or scattering-type scanning near-field optical microscopy (s-SNOM) [1–5] is a nondestructive optical imaging technique which circumvents the diffraction imposed resolution limit with the aid of strong field concentration at the apex of illuminated scanning probe tips [6–9]. Optical imaging is performed by recording the electromagnetic field E_{sca} scattered by the vibrating probe placed in the proximity of the specimen surface (Fig. 1a). The amplitude and phase of E_{sca} depend on the near-field interaction between the probe and the sample surface. Owing to this effect, highly resolved optical maps of the sample surface can be obtained by scanning a s-SNOM probe along the specimen surface. The attainable spatial resolution is determined by the sharpness of the probing tip, thus being independent of the illumination wavelength [10]. The remarkable material specificity of the near-field optical maps - particularly at infrared frequencies - makes s-SNOM a highly valuable analytical method for non-destructive mapping of chemical [5, 11–13], structural[14, 15], and conduction [16–18] properties on the nanometer scale.

In order to explain and predict the observed s-SNOM contrast, it is crucial to understand the

optical near-field (NF) interaction between the probing tip and the sample surface. Moreover, a quantitative model of the NF interaction would provide a key to unambiguous material identification based on near-field spectra and optical resonances. Earlier attempts at describing the NF interaction are based on a point-dipole model [5, 19–24] which is sufficient for a *qualitative* explanation of many phenomena experimentally observed in s-SNOM. They include material contrasts [11–15, 17, 25–27] as well as the phonon-polariton resonant NF interaction [28] and its blue-shift with increasing probe-sample distance [29]. However, the point-dipole model does not provide a good *quantitative* description of the measured near-field contrasts. Notable failings include the incapability to correctly reproduce near-field approach curves [30] as well as the spectral position, width and magnitude of polariton-resonant probe-sample NF interaction [14, 15, 28] which permits nanoscale-resolved optical analysis of polar crystals [14, 15], nanocomposites and semiconductor devices [18].

Numerical studies of the NF interaction between the tip and the sample employ different computational techniques, including finite element [7] and boundary element [31] methods, the multiple multipole method [32, 33], multipole expansion [34] and the finite difference time-domain approach [35]. However, numerical modeling of the tip-sample interaction usually requires great experience in carefully selecting compromises which are needed to make such demanding simulations computationally feasible. Numerical calculations also rarely take into account the probing tip vibration and higher harmonic signal demodulation, although they represent essential aspects of the s-SNOM signal detection [22, 36–38].

To our knowledge, no analytical or numerical model has so far quantitatively reproduced the experimentally observed material contrasts and spectra of resonant NF interaction [14, 15, 28]. With the constant improvement in the modelling techniques and computing power, it is likely that numerical methods will eventually succeed in this task. However, it is not likely that they will be fast enough to routinely determine the local dielectric function of a sample at each pixel in a recorded s-SNOM image. We therefore regard a model allowing a fast and accurate calculation of s-SNOM contrasts as an essential step towards this goal.

In this article we propose a novel model for describing material contrasts in infrared s-SNOM. Although several approximations are necessary to obtain an analytical solution, the model calculations yield an unprecedented agreement with experimental data.

In our finite-dipole model the s-SNOM probe (Fig. 1(a)) is represented by an isolated spheroid [19, 32, 33, 39–42] since this is the best known approximation that can be solved analytically. The illuminating field E_0 is assumed to be uniform and perpendicular to the sample surface and the spheroid much smaller than the wavelength (Fig. 1(b)). To derive an analytical expression for the NF interaction strength and the amplitude of the scattered field, in Section 2.1 we first examine the behavior of a perfectly conducting spheroid (PCS) in a uniform electric field E_0 in the absence of a sample. Electrostatic calculations indicate that the spheroid near-fields induced by E_0 can be approximated by the field of two point charges (monopoles) Q_0 and $-Q_0$ located close to its ends, as can be seen in Fig. 2.

We next consider the situation where a flat sample is located close to the spheroid apex. Because of the rapid decay of the monopole fields, we assume that only the charge Q_0 and its mirror image Q_0' give rise to a near-field interaction between the spheroid and the sample. In Section 2.2 we thus study the response of a spheroid to an external point charge, later representing the mirror charge in the sample. Based on the results of Section 2.2, we introduce an extended dipole p_i to account for the spheroid polarization induced by the NF interaction. Of the two point charges Q_i and $-Q_i$ constituting the dipole p_i, only the one closer to the sample (Q_i) is assumed to participate in the NF interaction. The existence of the opposite charge ($-Q_i$) is required by the electric neutrality of the spheroid and for forming the dipole p_i which emits electromagnetic (EM) radiation.

In Section 2.3, the approximate value and location of Q_i and $-Q_i$ are derived, enabling us to find a set of equations which determine the NF interaction strength. In Section 2.4 an expression for the electric field scattered by the probe is provided, from which the s-SNOM signals can be derived. In Section 3 the results of our model are compared to near-field approach curves and spectra of phonon-polariton resonant NF interaction obtained with an infrared s-SNOM. We further compare the results with the commonly used point-dipole model (Fig. 1(c)). While the point-dipole model provides a good qualitative description of the near-field interaction, it cannot satisfactorily reproduce the exact spectral position and contrast obtained in the experiments [15, 28, 29]. In contrast, the new finite-dipole model solves this problem by introducing an elongated tip and approximating it by a more accurate and versatile distribution of charge near its end.
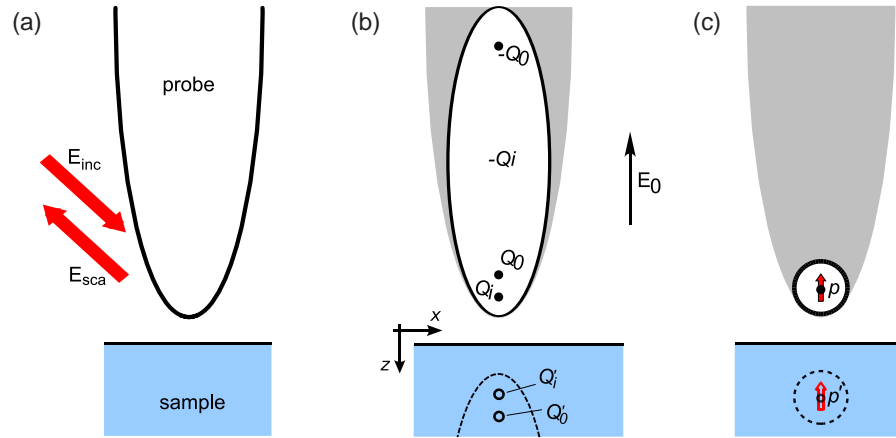

Fig. 1. Comparison of a typical s-SNOM probe-sample configuration with the finite-dipole and the point-dipole model. (a) The probing tip is typically an elongated structure illuminated by plain waves from the side. (b) In the finite-dipole model the tip is approximated by a spheroid in a uniform electric field $\mathbf{E}_0$. (c) In the point dipole model the tip is first reduced to a small sphere in an uniform electric field E_0. The sphere is then further reduced to a point dipole located in its center. The scattered field is finally calculated from a dipolar near-field coupling with the sample.

2. Finite-dipole model of the probe-sample near-field interaction

2.1. Monopole approximation of the probing tip near fields

As a first step towards an analytical description of the NF interaction between the spheroid and the sample surface, it will be shown that the near fields at the PCS apex can be approximated by the field of a monopole located in the center of curvature of the spheroid apex. Note that the illumination can be represented by a homogeneous field only for spheroids much smaller than the wavelength. For larger spheroids the strength of the near fields would be significantly overestimated in an electrostatic calculation due to the neglected dephasing effects. This fact restricts the possible length of the spheroids in our model to below $\lambda/4$ [32, 43].

In the electrostatic case, the electric field outside the spheroid and along its major axis is given by $E(D) = E_s(D) + E_0$ where E_0 is the illumination field, E_s the field generated by the spheroid, and D the distance from the spheroid apex. In the absence of a sample, the electrostatic

calculation for an isolated spheroid yields

$$E_s(D) = \frac{\frac{2F(L+D)}{D^2+L(2D+R)} + \ln\frac{L-F+D}{L+F+D}}{2\frac{F(L-\varepsilon_t R)}{LR(\varepsilon_t-1)} - \ln\frac{L-F}{L+F}} E_0, \tag{1}$$

with F being half the distance between the spheroid foci, R the radius of curvature at the apex and ε_t the dielectric function of the tip material [41, 42]. As well known, the field E_s increases with L/R.

When the spheroid is located above a surface, it is additionally illuminated by its reflected near fields (Eq. 1). Unfortunately, a closed-form solution describing the response of a spheroid in such a situation in not known. However, as this is necessary for calculating the near-field interaction, we have to find a simpler representation of the spheroid near fields. We therefore take a closer look at the electric field distribution of a spheroid.
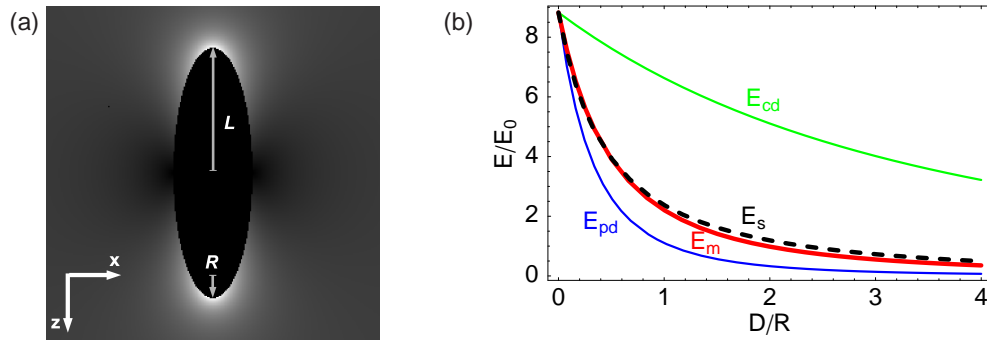

Fig. 2. (a) Electric field E_s around a perfectly conducting spheroid ($\varepsilon \to \infty$) with $R = 0.1L$ located in a homogeneous external field E_0 oriented along the spheroid's major axis. (b) Electric field of the spheroid as a function of the distance D from the spheroid apex along the z-axis. Shown are the exact result E_s from Eq. 1 (dashed line), the monopole field E_m (red line), point-dipole field E_{pd} (blue line), and field of a point dipole at the center of the spheroid, E_{cd} (green line), all scaled to the exact value E_s at the spheroid surface ($D = 0$).

From Fig. 2(a) it is obvious that the near field around the spheroid looks much like a field of a spatially extended dipole with the constituent charges residing close to the opposite ends of the spheroid. Consequently, the near field close to the apex can be approximated by a monopole field, as we show below. We note here that in contrast to the corresponding far field [44], the near field of an elongated spheroid cannot be described by a point dipole located in the spheroid center unless the spheroid is actually a sphere.

In Fig. 2(b) we compare the exact solution $E_s(D)$ with the field $E_{cd} = A_{cd}/(R+D)^3$ of a point dipole located in the center of a spheroid ($R/L = 0.1$), the field $E_m = A_m/(R+D)^2$ of a monopole located in the center of curvature of the spheroid apex and the field $E_{pd} = A_{pd}/(R+D)^3$ of a point dipole located in the center of a sphere inscribed into the tip apex. The constants A_{cd}, A_m and A_{pd} have been chosen such that fields at the spheroid apex ($D = 0$) match the exact value $E_s(0)$, i.e. such that $E_{pd}(0) = E_{cd}(0) = E_m(0) = E_s(0)$. We find that both dipole fields significantly deviate from E_s while the monopole field E_m yields a good quantitative approximation of the spheroid near field E_s. In the following we describe therefore the near field at the spheroid apex by a monopole to which we assign a charge Q_0.

2.2. Spheroid in an external monopole field

In order to calculate the near-field interaction between the probe and the surface, we describe the response of the sample to the spheroid's near fields by a mirror charge $Q_0' = -\beta Q_0$, where the electrostatic reflection factor

$$\beta = \frac{\varepsilon_s - 1}{\varepsilon_s + 1} \qquad (2)$$

is a function of the dielectric function ε_s of the sample [45]. The field generated by the charge Q_0' acts back on the probe, thereby polarizing it [46]. The amount and distribution of the induced charge needs to be known before we can calculate the near-field interaction strength. To simplify the mathematical treatment of the problem, we first consider the behavior of a spheroid that is grounded. When an external point charge Q_e (later being the mirror charge induced in the sample) is residing at a position $z_e > L$ (Fig. 3(a)), the totally induced charge Q_t on a grounded spheroid is given by [42, 47]

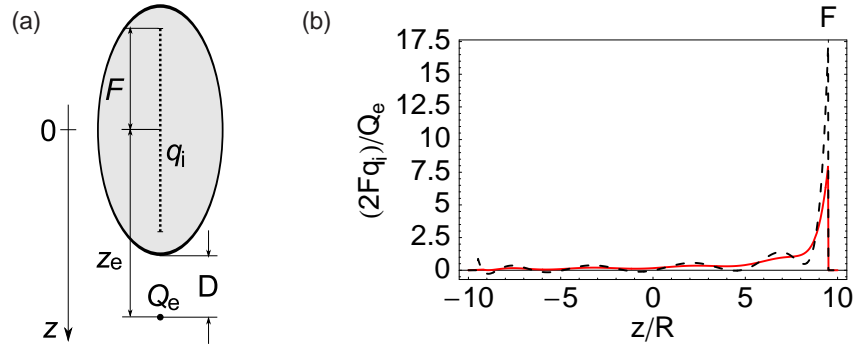$$Q_t = -Q_e \frac{\ln \frac{L+F+D}{L-F+D}}{\ln \frac{L+F}{L-F}}. \qquad (3)$$

Fig. 3. (a) The electric potential outside a grounded perfectly conducting spheroid in the presence of an external charge Q_e is equivalent to the potential of a certain non-uniform line charge distribution q_i. (b) Line charge distribution q_i induced along the axis of $\frac{R}{L} = 0.1$ spheroid as calculated from the first 10 terms in Eq. 4. The external point charge is located at $D = 2R$ (dashed line) and $D = 3R$ (full line).

From Fig. 4(a) we learn that Q_t increases towards the value of Q_e when the charge Q_e approaches the spheroid boundary. Furthermore, at a given distance D, more charge Q_t is induced when the ratio L/R increases. Thus, with increasing L not only the field E_s increases (Eq. 1), but also the near-field coupling with the sample surface becomes stronger.

To quantify the contribution of the induced charge Q_t to the NF interaction, it is necessary to investigate how Q_t is distributed over the spheroid. In [46, 48] it has been shown that the response of a grounded, perfectly conducting spheroid to Q_e is equivalent to that of a line charge distribution $q_i(z)$ along the line connecting the two spheroid foci (Fig. 3(a)). This charge distribution is given by the series

$$q_i(z) = -\frac{Q_e \Theta(F^2 - z^2)}{2F} \sum_{n=0}^{\infty} (2n+1) \frac{Q_n((L+D)/F) P_n(L/F)}{Q_n(L/F)} P_n(z/F) \qquad (4)$$

with Θ being the unit step function, Q_n the n-th order Legendre functions of the second kind, and P_n the Legendre polynomials [46]. The two examples of $q_i(z)$ displayed in Fig. 3(b) clearly

show that the amount and distribution of the induced charge depend on the distance D of the external charge Q_e while the highest charge density is found at the spheroid focus ($z = F$), i.e. at a distance $R/2$ (for $R \ll L$) from the spheroid apex.

2.3. Spheroid-sample near-field interaction

To be able to calculate the near-field interaction between the spheroid and the sample surface analytically, we replace the exact charge distribution q_i by an effective point charge Q_i. Since the density of the line charge q_i is highest in the spheroid's focus, we fix the location of Q_i to $z = F$. When the spheroid is in contact with the sample surface, mainly the charges in the immediate proximity of the contact area (i.e. in the spheroid apex) contribute to the near-field interaction. However, with increasing distance D between the spheroid and the sample surface, the relative contribution of charges further away from the tip apex increases. We thus assign to Q_i the charge located within the spheroid between $z = L$ and $z = L - (R + D)$:

$$Q_i = g\,Q_t = \int_{L-(R+D)}^{L} q_i(z)\mathrm{d}z \qquad (5)$$

The fraction $g = Q_i(D)/Q_t(D)$ is shown in Fig. 4(b). We observe a similar behavior for different spheroid shapes and furthermore that g is roughly constant for $D > R/2$. A reasonable estimate for this constant seems to be $g = 0.7 \pm 0.1$.
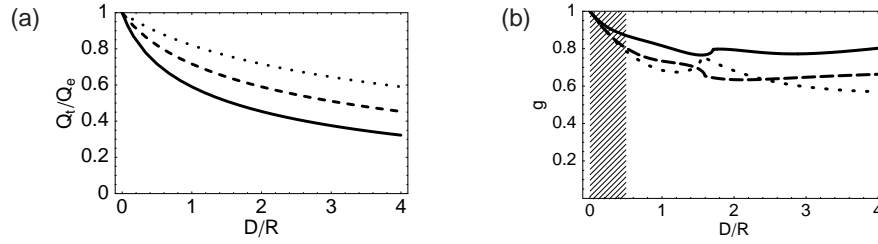

Fig. 4. (a) Totally induced charge Q_t, calculated for spheroids with $\frac{R}{L} = 0.2$ (full line), $\frac{R}{L} = 0.1$ (dashed) and $\frac{R}{L} = 0.05$ (dotted). (b) Fraction g of the totally induced charge Q_t found within the range $R + D$ from the tip end. Three different shape factor are shown: $\frac{R}{L} = 0.2$ (full line), $\frac{R}{L} = 0.1$ (dashed), and $\frac{R}{L} = 0.05$ (dotted). For $D/R \gtrsim 1.5$ the calculation was done according to Eq. 4. As for $D/R \lesssim 1.5$ the solution of Eq. 4 exhibits convergence problems, an improved theory with better numerical behavior was used [46]. There the charge distribution is represented by a line charge plus a point charges located between the tip and the focus of each spheroid apex. Note that the shaded region between $D = 0$ and $D = 0.5R$ represents distances which are not encountered in the model.

Up to now we have considered grounded spheroids, where the surplus charge $-Q_t$ is assumed to flow out. For an isolated spheroid (as assumed in our model, Fig. 1(b)) Q_i has to be modified since the surplus charge cannot leave the spheroid, but rather distributes in such a way that the entire surface of the spheroid remains equipotential. This requirement is satisfied when any slice of thickness Δz perpendicular to the z-axis contains an equal amount of charge, $\Delta Q = -Q_t\Delta z/(2L)$ [49]. To account for this charge, we have to replace the factor g by $g' = g - (R + D)/(2L)$. We obtain

$$Q_i = g'Q_t = (g - \frac{R+D}{2L})Q_t \,. \qquad (6)$$

It should be noted that when the spheroid above a flat surface is illuminated with an external field E_0 the induced charge Q_i actually consists of two parts:

$$Q_i = Q_{i,0} + Q_{i,1}. \tag{7}$$

For $Q_{i,0}$, the external charge Q_e is the mirror image Q'_0. For $Q_{i,1}$, the external charge Q_e is the mirror image of Q_i itself which is denoted in the following by Q'_i. The corresponding distances D_0 and D_1 are easily read from Fig. 5:

$$
\begin{aligned}
D_0 &= 2H + R \text{ and}\\
D_1 &= 2H + \frac{R}{2},
\end{aligned}
\tag{8}
$$

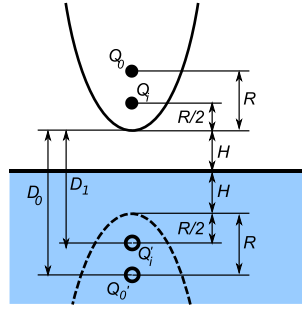where H denotes the distance between the spheroid apex and the sample surface.

Fig. 5. Charges participating in the near-field interaction between the probe and the sample, together with their positions according to the finite-dipole model.

Inserting Eqs. 8 into Eq. 6 and neglecting $R/2$ and D in comparison to $2L$, the following relations between the image charges Q'_0 and Q'_i and the monopoles $Q_{i,0}$ and $Q_{i,1}$ they induce in the probe are obtained:

$$
\begin{aligned}
Q_{i,0} &= f_0 Q'_0 = -(g - \frac{R+H}{L}) \frac{\ln \frac{4L}{4H+3R}}{\ln \frac{4L}{R}} Q'_0\\
Q_{i,1} &= f_1 Q'_i = -(g - \frac{3R+4H}{4L}) \frac{\ln \frac{2L}{2H+R}}{\ln \frac{4L}{R}} Q'_i.
\end{aligned}
\tag{9}
$$

The total induced charge Q_i is a measure for the strength of the near-field interaction between the probe and the sample.

The image charges Q'_0 and Q'_i can be written as

$$
\begin{aligned}
Q'_0 &= -\beta Q_0\\
Q'_i &= -\beta Q_i.
\end{aligned}
\tag{10}
$$

As the monopole Q_i comprises $Q_{i,1}$ which is proportional to the mirror image of Q_i itself, we have obtained a recursive definition for Q_i which can be solved by searching for a self-consistent solution. Inserting Q'_0 and Q'_i from Eq. 10 into Eq. 9 we get

$$Q_i = \frac{-\beta f_0}{1 + \beta f_1} Q_0. \tag{11}$$

This allows a dimensionless "near-field contrast factor" $\eta = Q_i/Q_0$ to be defined as an illumination-independent measure of the s-SNOM signal, comparable between different samples and different measurements:

$$\eta = \frac{Q_i}{Q_0} = \frac{\beta \left(g - \frac{R+H}{L}\right) \ln \frac{4L}{4H+3R}}{\ln \frac{4L}{R} - \beta \left(g - \frac{3R+4H}{4L}\right) \ln \frac{2L}{2H+R}} . \tag{12}$$

2.4. Light scattering by the probe and effective probe polarizability

In a typical s-SNOM experiment, the light scattered from the probe is detected. We thus have to describe how the scattered field E_{sca} depends on the near-field interaction i.e. the near-field contrast factor η. In this regard we again note that the electric neutrality of an isolated spheroid requires the existence of a charge $-Q_i$ somewhere on the spheroid. For this reason we can assign a dipole moment p_i to the total charge distribution oscillating with the driving field frequency. p_i radiates light according to the general expression $E_{sca} \sim p = \alpha E_0$ with α being the dipole polarizability.

The dipole moment p_i can be easily derived by considering that the charge -Q_i must not break the equipotential property of the spheroid. For symmetry reasons we thus can locate the total amount of $-Q_i$ into the spheroid center yielding $p_i = Q_i L$. Subsequently, the effective dipole moment of the perfectly conducting spheroid is given by $p_{\mathrm{eff}} = p_0 + p_i$, where $p_0 = 2Q_0 L$ is the dipole moment induced by the external field E_0 and $p_i = \eta Q_0 L$ the dipole moment arising from the near-field interaction. From the monopole approximation of the spheroid field E_s (Eq. 1) we obtain $Q_0 = R^2 E_s(0)$ and the effective probe polarizability α_{eff} in the case $R \ll L$:

$$\alpha_{\mathrm{eff}} = \frac{p_{\mathrm{eff}}}{E_0} = R^2 L \frac{\frac{2L}{R} + \ln \frac{R}{4eL}}{\ln \frac{4L}{e^2}} \left(2 + \frac{\beta \left(g - \frac{R+H}{L}\right) \ln \frac{4L}{4H+3R}}{\ln \frac{4L}{R} - \beta \left(g - \frac{3R+4H}{4L}\right) \ln \frac{2L}{2H+R}}\right). \tag{13}$$

Eq. 13 can be directly compared to the effective probe polarizability

$$\alpha_{\mathrm{effpd}} = \frac{\alpha}{1 - \frac{\alpha\beta}{16\pi(R+H)^3}} \tag{14}$$

obtained from the point-dipole model (Fig. 1(c), [4, 22]). Here $\alpha = 4\pi R^3$ is the polarizability of a perfectly conducting sphere, R the radius of the sphere, and H distance between the sphere and the sample surface.

To obtain the final expression for the scattered field we have to take into account that the probe in an experimental situation is illuminated by the incoming field E_{inc} directly and indirectly due to its reflection at the sample surface (Fig. 6). Furthermore, the scattered field is also reflected at the sample surface [25]. For simplicity, we shall assume that both the plane wave illumination and the backscattering are in the same direction. Although the incoming field may have both x- and z-components, due to the strong depolarization by the probing tip we can neglect the x-, and consider only the z-component of the incoming field, as assumed in the model. According to this assumption, we can write the field scattered from the probe (i.e. from the effective dipole p_{eff}) as

$$E_{\mathrm{sca}} \propto (1 + r_p)^2 \alpha_{\mathrm{eff}} E_{\mathrm{inc}}, \tag{15}$$

with r_p being the Fresnel reflection coefficient for p-polarized light.

We should point out here that in former applications [4, 14, 15, 22, 26, 28, 30, 50] of the point-dipole model the scattered field was described differently, by

$$E_{\text{sca}} \sim \frac{\alpha(1+\beta)}{1 - \frac{\alpha\beta}{16\pi(R+H)^3}} E_{\text{inc}} = (1+\beta)\,\alpha_{\text{effpd}}\,E_{\text{inc}} \tag{16}$$

where the factor $(1+\beta)$ appears instead of $(1+r_p)^2$. First, the indirect probe illumination by reflection at the sample surface is not taken into account in Eq. 16, which was already noted in [25, 33]. Secondly, the scattered light reflected at the sample surface, $E_{\text{sca,r}} \sim r\,\alpha_{\text{eff}}\,E_{inc}$, is represented by light scattering of the mirror dipole $p'_{\text{eff}} = \beta\,p_{\text{eff}}$ yielding $E_{\text{sca,r}} \sim \beta\,\alpha_{\text{effpd}}\,E_{\text{inc}}$. Here it is important to note that the electrostatic reflection coefficient β can be applied for calculating the near-field interaction between the probe dipole and the sample, as well as the resulting near fields. However, it can not be applied for describing the reflection of the propagating fields emitted by the effective probe dipole [42, 51]. As β can be larger than unity, this situation would not conserve energy. Therefore Eq. 15, rather than Eq. 16 should be employed in the future, independent of the underlying model used for describing the near-field interaction.

2.5. Parameters of the model

Three of the five quantities encountered in Eq. 12 are easy to determine since β is defined in terms of the dielectric function ε_s (Eq. 2) while the tip radius R and the tip-sample separation H can be measured in the experiment. On the other hand, the effective spheroid length L and the factor g are not directly measurable, and theoretical considerations give only some constraints on their values. In particular, the probe length $2L$ must be much smaller than the wavelength due to the electrostatic approximation. The least precisely defined parameter is the factor g, related to the proportion of the total induced charge Q_t that is relevant for the near-field interaction. It was replaced by a constant estimated to about 0.7 ± 0.1 based on Fig. 4. In practice, some corrections can be incorporated into the factor g on a phenomenological basis, such as the effect of using a probe with finite conductivity instead of a perfectly conducting spheroid. Further corrections may also include the radiation resistance which has been neglected so far. Given that the near-field coupling is essentially capacitive in its nature, the electric resistance due to finite conductivity and the radiation resistance cause a slight phase difference between the driving field and the response of the probe. This phase difference may be accounted for by using a complex factor g with a small imaginary component.

In the absence of other means to obtain g and L, they were determined by searching for values which are in a good agreement with the available experimental data presented in Section 3, including approach curves and near-field spectra of phonon-polariton resonant samples. According to our inspection, the best values found are $g = 0.7e^{0.06i}$ and $L = 300$ nm. It is thereby important to note that the same values of these parameters will be subsequently used for all comparisons to the measured data, i.e. they are not adjusted to each experiment separately.

3. Experiment vs. finite-dipole model

In this section we compare our model quantitatively with mid-infrared s-SNOM data. After describing the microscope and experimental details we analyze approach curves on a flat gold surface and spectra of phonon-polariton resonant near-field interaction with a flat SiC surface.

3.1. Microscope setup and experimental details

Our infrared s-SNOM is based on a non-contact atomic force microscope (AFM, tapping frequency Ω, tapping amplitude $\Delta z \approx 20$ nm, tip radius $a \approx 20$ nm) where cantilevered Pt-coated tips act as scattering probes [4]. It operates with different CO_2-lasers covering the spectral region from $880\,\text{cm}^{-1}$ to $1100\,\text{cm}^{-1}$. A parabolic mirror is used for illuminating the tip with the

laser radiation and to collect the back scattered light. Interferometric detection of the scattered light together with demodulation of the detector signal at a frequency $n\Omega$ with $n > 1$ (higher harmonic demodulation) allows the unavoidable background scattering to be suppressed. By phase modulation of the reference beam (pseudo-heterodyne detection) we obtain amplitude s_n and phase ϕ_n signals simultaneously and avoid the interferometric background effect [52].

In our model the higher harmonic demodulation [36, 37, 53, 54] can be taken into account by Fourier decomposition of the time-dependent scattered field $E_{sca} = E_{sca}[z(t)]$, yielding the demodulated optical signal

$$E_n = s_n e^{i\phi_n} \sim (1 + r_p)^2 \alpha_{eff,n} E_{inc}. \tag{17}$$

where $z(t) = \Delta z \sin \Omega t$ describes a sinusoidal tip motion.

From the s-SNOM amplitude and phase images we usually extract material contrasts rather than the absolute values. A typical experimental situation is shown in Fig. 6 where the tip scans a sharp boundary between the materials A and B. In the case where we measure s_n and ϕ_n very close to the material boundary, we can assume that the reflection coefficient r_p does not change when the probing tip moves from surface A to surface B. The amplitude and phase contrasts are then given by

$$\frac{s_{n,A}}{s_{n,B}} = \left| \frac{(1 + r_A)^2 \alpha_{eff,n,A}}{(1 + r_A)^2 \alpha_{eff,n,B}} \right| = \left| \frac{\alpha_{eff,n,A}}{\alpha_{eff,n,B}} \right| \tag{18}$$

and

$$\frac{\phi_{n,A}}{\phi_{n,B}} = \arg \left(\frac{(1 + r_A)^2 \alpha_{eff,n,A}}{(1 + r_A)^2 \alpha_{eff,n,B}} \right) = \arg \left(\frac{\alpha_{eff,n,A}}{\alpha_{eff,n,B}} \right). \tag{19}$$

Note that the calculation with the finite-dipole model can be simplified for $n > 0$ by substituting the ratio $\alpha_{eff,n,A}/\alpha_{eff,n,B}$ by $\eta_{n,A}/\eta_{n,B}$ since α_{eff} (Eq. 13) and η (Eq. 12) differ by constant term and constant factor only.
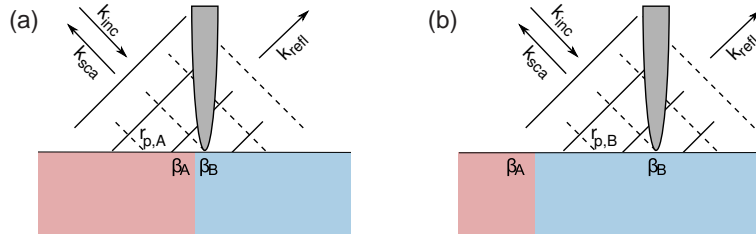

Fig. 6. Choosing the far-field reflection coefficient r_p. (a) Probe close to the material boundary: $r_p \approx r_{p,A}$, (b) Probe far from the material boundary: $r_p = r_{p,B}$.

3.2. Approach curves on a Au sample

In Fig. 7 we show approach curves measured by s-SNOM on a flat Au film. They are obtained by switching off the closed-loop distance control of the AFM and moving the sample away from the vibrating tip. The symbols in Fig. 7(a) show the amplitude signal s_2 averaged over 100 single approach curves. The measurements were carried out with a Pt-coated Si tip (Nanosensors, PPP-NCHPt) which radius $R = 20$ nm was estimated from the topographical resolution. The measured tip vibration amplitude was $A = 18$ nm. The theoretical curve (solid line in Fig. 7(a)) was calculated according to our model using $g = 0.7 e^{0.06i}$ and $L = 300$ nm. We find an excellent quantitative agreement. The point-dipole model in contrast predicts a much faster decay of the

signal with D (dashed line in Fig. 7(a)). This is not surprising as the decay of the dipole field (D^{-3}) is much faster than that of a monopole (D^{-2}).

We note that the approach curves can be also fitted by a point-dipole model when the polarizability of a spheroid is assigned to the probe dipole located in its center. The ratio between the spheroid's major and minor axes is the fit parameter, while the apex curvature R is taken from the experiment [31]. Figure 7(b) shows the result of such a successful fit procedure. However, using the same fit parameter, this model fails to quantitatively reproduce the spectra of phonon-polariton resonant near-field interaction while our new model provides again an excellent agreement (Section 3.3).
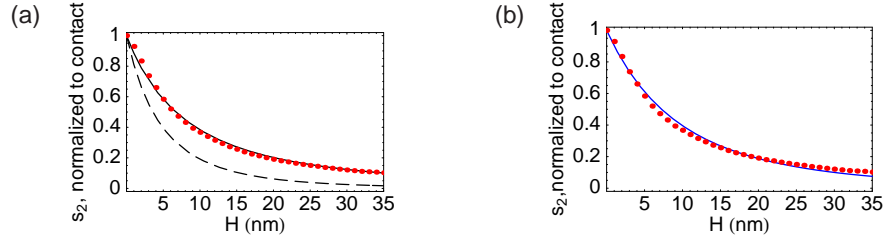

Fig. 7. Approach curves on a gold surface demodulated at the second harmonic ($n = 2$) of the modulation frequency. (a) Predictions by the finite-dipole model (full line) and the point-dipole model (dashed line) compared to the experimentally obtained values (dots). All values are normalized to the signal at $H = 0$. (b) Experimental approach curve (red dots) fitted by a dipole model, with ratio between the spheroid's semi-major and semi-minor axis being the fit parameter.

3.3. Near-field spectra of a phonon-polariton resonant SiC sample

One intriguing theoretical prediction of the point-dipole model is the existence of a near-field resonance when the real part of the dielectric function of the sample is close to $\varepsilon' \approx -2$, while the imaginary part is $\varepsilon'' \ll 1$. Because of $\beta = (\varepsilon - 1)/(\varepsilon + 1)$ the denominator in Eq. 14 becomes very small, which is also the case in our new model (Eq. 12). Such near-field resonances have been indeed observed with crystalline SiC samples when tuning the illumination wavelength from 9.2 μm to 11.2 μm [14, 15, 28]. The observed phenomenon can be attributed to phonon-enhanced near-field interaction as it relies on the resonant near-field excitation of crystal lattice vibrations in SiC. Similar resonances can be also observed with doped semiconductor samples where the near fields of the tip excite resonant electron oscillations [16–18]. As the position and the strength of those near-field resonances depend on the energies of the phonon (plasmon) modes in the examined crystals (semiconductors) they are highly specific to the chemical composition of the crystal and its structure (doping concentration), just like far-field infrared spectra. This provides the opportunity for infrared identification of crystals and their structural properties with a spatial resolution of about 20 nm ($\lambda/500$) [14, 15, 28] or the mapping of nanoscale doping gradients [18]. Although the point-dipole model qualitatively predicts such resonances, the quantitative agreement is not yet good enough for measurement of the local dielectric function.

Our results displayed in Fig. 8 show a comparison of the theoretically predicted (lines) and experimentally observed (symbols) near-field spectra of a 4H-SiC crystal which c-axis is oriented parallel to the surface. In contrast to the point-dipole model (dashed line, Eq. 14 and Eq. 15), the finite-dipole model (solid line, Eq. 13 and Eq. 16) shows an excellent agreement in both amplitude and phase, s_2 and ϕ_2. The only deviation is observable in the phase ϕ_2 at frequencies where the amplitude s_2 is low. It is difficult to tell whether this discrepancy should

be attributed to an error in the theory or in the experiment because the phase is very susceptible to random and systematic errors when the signal amplitude is low. In particular, the unsuppressed part of the background scattering may significantly alter the measured signal phase if the near-field signal is weak.

We note that in Fig 7(b) the point-dipole model could be fitted to approach curves on a Au sample. However, as an increased distance between the probe dipole and the surface is required to achieve this, the calculation of the SiC near-field spectra (Fig. 8, doted curve) yields a resonance shift to higher frequencies [29]. For this reason the point-dipole model can not fit approach curves and near-field spectra of polariton-resonant near-field interactions simultaneously.
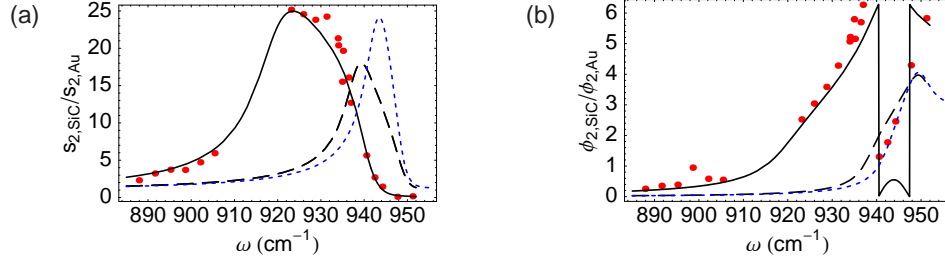

Fig. 8. Near-field spectra of a 4H-SiC crystal cut parallel to the c-axis. Signal demodulation was done at the second harmonic (n=2) of the tapping frequency. Shown are the experimental data (red dots) and the predictions by the finite-dipole model (solid line), the point-dipole model (dashed black line), and the point-dipole model employing the fit parameter as described in Section 3.2 (dashed blue line).

Having shown the result, we now provide more details of the experimental data acquisition and the calculation procedure. Both the experimental spectra and the calculations are normalized to a Au surface such that Eq. 18 and Eq. 19 apply. To perform a corresponding experiment we evaporated a 30 nm thick Au film onto the SiC crystal and acquired s-SNOM images of a sample area where the Au was partly removed by scratching. Amplitude s_2 and phase ϕ_2 values of SiC and Au were extracted within 200 nm distance from the sharp boundary between the two materials. To minimize the possibly disturbing excitation of surface phonon-polaritons on SiC at the material boundary [55], the sample was oriented such that the illumination direction was towards the Au film. The situation corresponds to Fig. 6(a) in case material A is the SiC and material B the Au film.

The calculation of the spectra was performed according to Eq. 13 (finite-dipole model, solid line) and Eq. 14 (point-dipole model, dashed line) employing experimental parameters for the tip radius $R \approx 35$nm (MikroMasch, CSC37/Ti-Pt) and the tip vibration amplitude $A = 25$nm. Note that the parameters $g = 0.7e^{0.06i}$ and $L = 300$nm were taken over from Section 3.2. They were *not* adjusted separately for the spectra. For the dielectric function of the undoped 4H-SiC we use the single harmonic oscillator model

$$\varepsilon(\omega) = \varepsilon_\infty + \frac{\varepsilon_\infty(\omega_{LO}^2 - \omega_{TO}^2)}{\omega_{TO}^2 - \omega^2 - i\gamma\omega} \tag{20}$$

where ω_{LO} is the longitudinal optical phonon frequency, ω_{TO} the transverse optical phonon frequency and γ the damping parameter. Because of the anisotropy of the 4H-SiC crystal, we have to consider that the electrostatic reflection factor β depends on the electric field orientation [56]. When the c-axis is parallel to the surface (as with our 4H-SiC sample), the evanescent fields with polarization perpendicular to the c-axis reflect with

$$\beta_\perp = \frac{\varepsilon_\perp - 1}{\varepsilon_\perp + 1}, \tag{21}$$

while the evanescent fields parallel to the c-axis reflect with

$$\beta_\parallel = \frac{\sqrt{\varepsilon_\perp \varepsilon_\parallel} - 1}{\sqrt{\varepsilon_\perp \varepsilon_\parallel} + 1}. \tag{22}$$

Due to the symmetry of the monopole/dipole field, all polarizations in the surface plane contribute equally to the near-field interaction. For the reflection factor β we thus assume an average electrostatic reflection factor

$$\beta = \frac{\beta_\perp + \beta_\parallel}{2}. \tag{23}$$

We calculate the values of $\varepsilon_\perp$ and $\varepsilon_\parallel$ from the literature data shown in Table 1:

	$E \parallel$ c	$E \perp$ c
ε_∞ [57]	6.78	6.56
ω_{TO} [58]	782 cm^{-1}	797 cm^{-1}
ω_{LO} [58]	967 cm^{-1}	971 cm^{-1}
γ [59]	6.6 cm^{-1}	6.6 cm^{-1}

Table 1. Literature data used for calculating the SiC dielectric function.

We note that Eq. 23 is an approximation of how the electrostatic field of a point charge reflects off an anisotropic crystal. A more complete treatment of this problem is given in Refs. [60–62] which could also be applied to our model in the future, especially for largely anisotropic materials. Due to a moderate anisotropy level in SiC, this is not deemed necessary here.

4. Conclusion

So far, nanoscale optical material characterization using s-SNOM has been limited by quantitative discrepancies between calculated and measured near-field optical contrasts. To overcome this problem, a new analytical model of the probe-sample interaction in s-SNOM has been derived in this article. Treating the probe as a prolate spheroid much smaller than the wavelength, we find that its near field is much better described by a finite dipole consisting of point charges Q_0 and $-Q_0$ rather than by the field a point dipole. The charge Q_0 residing close to the sample surface is assumed to induce the near-field interaction which further polarizes the spheroid. Approximating the corresponding charge redistribution by a point charge Q_i in the spheroid's focus and a uniform distribution of charge $-Q_i$ along the spheroid, we obtain a closed-form solution reproducing the experimental data. The degree of compliance with the experiment thereby depends on the model spheroid length, which was taken as a parameter and fitted to the experimental results. Interestingly, it was found to be $2L = 600\,\text{nm}$ which is smaller than the maximum length permitted by the underlying electrostatic approximation ($\lambda/4 \approx 2.5\,\mu\text{m}$). Future experiments or numerical studies are necessary to determine whether this is due to the neglected retardation and damping effects or whether the effective probe length is indeed much shorter than length of commonly used AFM tips ($L \geq 10\,\mu\text{m}$). In the latter case, employing shorter tips would be preferable as they would produce less background scattering [42]. The other parameter used in the model is the factor g. It determines the fraction of total charge induced in the spheroid that participates in the near-field interaction. While the real part of g was found by comparison with the exact solution for a spheroid in a monopole field, the imaginary part of g was introduced to account for the finite resistance of the probe and the radiation damping. Being very small ($\text{im}(g) \approx 0.04$), in practice it only affects the magnitude of the resonant

probe-sample near-field interactions, but not their spectral position. By extending our model to dielectric probes based on [46] and explicitly including the radiation damping, it should be possible to completely dispense with the imaginary part of g as a fit parameter. This would also enable the application of the model to visible wavelengths and to polariton-resonant probes. We note that both parameters g and L likely depend on the actual geometry of the probing tip. In our experiments we used Pt-coated Si tips rather than solid metal tips. As the skin depth of Pt at mid-IR frequencies ($\delta = \lambda/(2\pi \, \text{im}\sqrt{\varepsilon_{Pt}}) \approx 50$ nm with $\varepsilon_{Pt} = -1000+500i$ [63]) is larger than the thickness of the Pt-coating ($\approx$20 nm), we expect g and L also being dependent on the thickness of the coating.

Even in its present form, the finite-dipole model already promises the quantitative analysis of infrared s-SNOM images. Applied in the inverse way, it could allow the generation of nanoscale resolved maps of the dielectric function of the sample surface. Besides the chemical and structural identification, this could enable non-invasive measurements of properties such as the local strain and doping concentrations which are amongst the most important physical parameters in novel (opto-) electronic nanodevices. Another interesting application of the model would be the description of the probe-sample near-field interaction in the THz range. As typical AFM probes in that case are much shorter than the wavelength, their length could be directly employed in the model.

Acknowledgments